Scattering of ^{15}C on ^{208}Pb at energies near the Coulomb barrier: Study of the experimental device response via the ^{12}C+^{208}Pb scattering

*V.G.*Távora[1,*], *J.D.* Ovejas[1], *I.* Martel[2], *O.* Tengblad[1], *M.J.G.* Borge[1], *L.* Acosta[5], *T.* Kurtukian-Nieto[1], *A.M.* Sánchez-Benítez[2], *A.* di Pietro[3], *P.* Figuera[3], *N.* Keeley[4], *K.* Rusek[4], and the IS619 collaboration.

[1]Instituto de Estructura de la Materia, CISC, Serrano 113bis, E-28006 Madrid, Spain
[2]Departamento de Física Aplicada, Universidad de Huelva, E-21071, Huelva, Spain
[3]INFN, Laboratori Nazionali del Sud, via S. Sofia 62, 1-95123, Catania, Italy
[4]National Center for Nuclear Research, ul Andrzeja Soltana 7, 05-400 Otwock, Poland
[5]Instituto de Física, Universidad Nacional Autónoma de México, Mexico City, Mexico

Abstract. There are evidences that the ^{15}C nucleus has an extended neutron distribution or a "neutron halo", but this situation is far from clear. If ^{15}C has 1n-halo, the scattering dynamics should be affected and the angular distribution of the elastic channels should be sensitive to coupling effects due to the halo configuration. The objetive of this study is to understand the role of the halo in ^{15}C by investigating its dynamical response in intense electric fields at energies close to the Coulomb barrier. For this purpose experiment IS619 was conducted performing the ^{15}C + ^{208}Pb elastic scattering reaction at HIE-ISOLDE, CERN. The beam energy was 4.37 *MeV/u*, which is very close to the Coulomb barrier of the system. The experimental setup used was the global detection system GLORIA, a six silicon telescopes array enable to measure the energy and angular distributions of the scattered particles. During the experiment, the ^{12}C+^{208}Pb scattering at 4.37 *MeV/u* was measured for calibration. The results of the ^{12}C+^{208}Pb measurement were used to fine-tune the geometry of the experimental setup and it is presented in this contribution.

1 Introduction: neutron halos

Nuclear systems such as ^{6}He, ^{11}Li, ^{11}Be, ^{14}Be are known to have an extended neutron distributions: the so-called neutron halos [1, 2]. This feature occurs when the separation energy of valence neutrons is very low and certainly much smaller than the average binding energy per nucleon in a nucleus, so the valence neutrons can tunnel out of the nuclear potential to large distances with sizable probability. It has been an intense experimental and theoretical activity dedicated to study the existence of halos and their dynamics in reaction processes. The neutron halos produces a pronounced maxima at low excitation energies in the Coulomb dipole strength B(E1), very narrow transverse momentum distributions and large interaction cross-sections when measured at high energies [3].

The dynamics of the halo nuclei scattering at low energies, around the Coulomb barrier, is dominated by the coupling between the elastic channel and collective excitations, neutron transfer and breakup. The angular distributions of the elastic cross section and the core fragments present large sensitivity to these coupling effects, due to the halo configuration. This has been demonstrated in previous studies with light exotic beams of ^{6}He, ^{11}Li and ^{11}Be scattered on heavy targets [4–6]. The angular distribution of the elastic channel shows strong absorption patterns where the nuclear and Coulomb interference completely disappears.

The ^{15}C nucleus ($T_{1/2}$ = 2.449(5) *s*) has a low single neutron separation energy S_n = 1218.1(8) *keV* in comparison to the two-neutron separation energy S_{2n} = 9394.5(8) *keV* [7] and the neighbors ^{14}C (S_n = 8176.43 *keV*) ^{16}C (S_n = 4250 *keV*). The spins and parities of the ground and first excited state at E = 740 *keV* of ^{15}C are known to be $I_\pi = 1/2^+, 5/2^+$, respectively.

The halo structure of ^{15}C has been investigated at relatively high energies in several experiments. The reaction cross section at 83 *MeV/u* shows an enhancement respect to the neighboring ^{14,16}C isotopes [8], and the longitudinal momenta of the ^{14}C fragments after 1n-breakup present a FWHM distribution between 64-70 *MeV/c* depending of the target that it is narrower than that of the neighbour ^{14,16}C isotopes, $\sim$ 200 *MeV/c*, but wider than the typical $\sim$ 40-50 *MeV/c* found for the archetype cases [3]. These properties have hinted the presence of a 1n-halo configuration in the ^{15}C nucleus that would be unique in the sense that it can be described with an almost pure $s_{1/2}$ ground state wavefunction [8].

On the other hand, the enhancement of the cross section observed at 83 *MeV/u* is not seen at 950 *MeV/u* [8]. Also nuclear matter radii and density were revisited in [9] obtaining a value of $\kappa = R_v/R_c = 1.81$ for the ratio between radius of the valence neutron and core radius distribution, where $\kappa > 2$ for typical halo nucleus.

To complete the understanding of the role of the halo in ^{15}C, its dynamical response at energies close to the Coulomb barrier has been studied in IS619 experiment,

*e-mail: vicente.garcia@csic.es

where, according with [10, 11], a scattering dominated by the competition of 1n-stripping and breakup is expected.

A ^{12}C beam at the same energy per nucleon was measured with the same ^{208}Pb targets for calibration of the experimental device.

2 Experimental Methodology

The study of ^{15}C +^{208}Pb elastic scattering was performed at HIE-ISOLDE, CERN. Where the ^{15}C beam was produced from the impact of 1.4 GeV proton pulses on a CaO production target. The isotope of interest was extracted, mass-separated and post-accelerated to 4.37 *MeV/u*, which is very close to the Coulomb barrier of the system.

The radioactive beam impacted on a target of ^{208}Pb with purity higher than 98% and two different thicknesses; one of 2.1 and the other of 1.2 mg/cm^2. Using the thicker target, the energy losses increased but favors a higher amount of reactions and more statistics. Using the thin target the statistics decreased but there was less straggling, and better energy resolution.

The experimental setup for IS619 was the global reaction array, called GLORIA [12]. It consisted of 6 silicon telescopes, all tangent to a 6 cm radius sphere in which center the reaction target was placed. All telescopes were composed of a 40 μm ΔE detector and a 1 *mm* E detector. Both detectors had 16x16 strips, which means that they worked as a set of 256 pixels each with an angular resolution between 2 and 3º. Dynamic ranges were adjusted to around 50 *MeV* to detect the scattered ^{15}C ions at ~ 65 MeV lab. energy. The system had an angular coverage from 15 to 165º in a continous way with some overlapping areas between pairs of telescopes. The geometric efficiency was 25% of 4π. The detector resolution was in the order of 30 *keV* FWHM.

A scheme of this configuration is presented in Fig. 1 as well as the nominal angular range covered by each detector in Tab. 1. The target ladder was placed with a 30º tilt respect to the beam direction, this avoids shadowing at 90º but introduces an asymmetry in the energy losses through the azimutal angle. The telescope C did not work during the experiment.

Table 1. The angular coverage of the six telescopes is given. Center of the detectors, geometric angle range for each telescope is given assuming that beam and target were centered and the final effective angular coverage.

Telescope	Center (º)	Geometric angular range (º)	Effective angular range (º)
A	38	15-62	23-58
B	38	15-62	22-57
F	75	52-97	59-95
E	105	82-128	91-124
D	142	117-165	123-154
C	142	117-165	

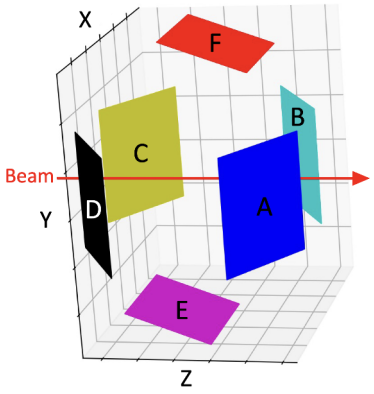

Figure 1. Schematic representation of the telescope configuration used during the experiment.

3 Analysis procedure

For single particle detection in double-sided detectors, the junction (P-side) and the ohmic (N-side) are read separately. For good events, these signals correspond to the same deposited energy. Experimentally a certain deviation between both sides is expected, so the $|E_p - E_n| \leq 2\sigma$ condition has been included in the data processing, where σ value is obtained from the gaussian fit applied to $|E_p - E_n|$ distribution for each detector, either front detector, ΔE, or back detector, E.

As it is explained in [13], the beam is not polarised so the reaction fragments follow axial symmetry and the same physics is expected to happen over the same dispersion angle θ. Due to that symmetry, the scattering for each θ-angle follows a conical surface. This property allow the grouping of all the pixels that belong to a determined angular sector ($\Delta\theta$) (Fig. 2 left).

The ΔE-E telescope configuration makes possible ion identification (Fig. 2 right), hence, those events can be selected by a gate in the corresponding range of the ^{15}C elastic scattering events. The border strips of both detectors of each telescope were removed due to the lower coincidence efficiency.

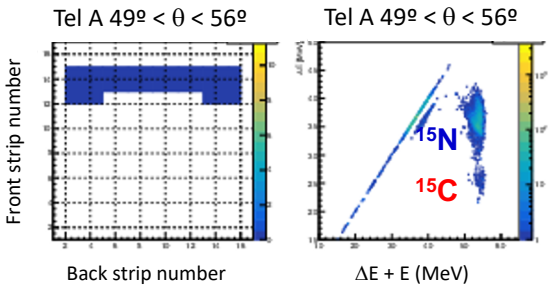

Figure 2. On the left hand side, the pixels selected in the angular coverage 49º< θ < 56º are shown. On the right hand side, the ΔE-E plot where the contaminant ^{15}N and the beam ^{15}C are clearly separated.

3.1 ^{12}C+^{208}Pb elastic scattering

The comparison performed between ^{15}C Rutherford cross section and the experimental cross section of ^{15}C elastic scattering on lead given in [13] shows large error bars hampering any conclusion about the dynamic behaviour of ^{15}C beam on heavy targets. In [13], the geometry optimization was done using the stable ^{15}N present in the beam.

In addition, the ^{12}C+^{208}Pb scattering was measured under the same conditions described in section 2. At these energies, a pure elastic scattering behavior is expected for ^{12}C. This can be used as an additional set of data to check the optimization of the geometry made in [13] and to normalize the distribution of the cross section obtained for ^{15}C+^{208}Pb by the elastic scattering of the stable isotope. ^{12}C+^{208}Pb data were treated with the same procedure explained in sections 3.

The angular distribution of the ratio between $\sigma_{^{12}C+^{208}Pb}$ and σ_{Ruth} is presented in Fig. 3. With $\sigma_{^{12}C} = I_{pixel}/\Omega_{pixel}$ and $\sigma_{Rutherford} = N/\sin^4(\theta_{pixel}/2)$, where I_{pixel} is the integral of ^{12}C ions for each pixel, N is the normalization constant, Ω_{pixel} and θ_{pixel} are the solid angle and scattering angle subtended for each pixel respectively.

Despite the efforts dedicated to the alignment of the chamber and detectors, a small shift ($\sim mm$) on the reaction point or a tilt of the beam direction is always expected. This results on small deviations of the solid angles Ω and angles (θ, ϕ) of each pixel of the detectors due to the very close geometry of the setup so, a cloud of points with small deviations around 1 was expected due to the pure elastic scattering reaction of ^{12}C. In this case, a wide distribution of the points is shown in Fig. 3 where a clear upward trend can be observed in the data-sets for each telescope, in addition to the lack of continuity for the intersection zones between telescopes and the lack of symmetry for mirror telescopes A and B. This behavior indicates the need for further geometry optimization to be performed.

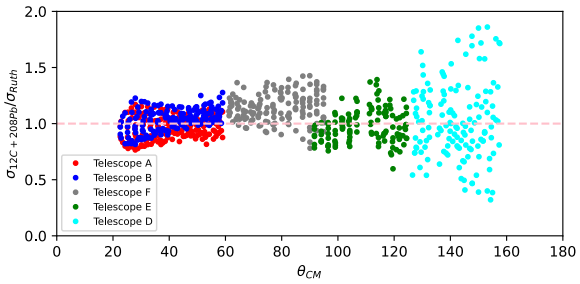

Figure 3. Differential elastic scattering of ^{12}C +^{208} Pb. The data per pixel shows large dispersion angular distribution that indicates thar a geometrical optimization is needed.

4 Geometry optimization

To carry out the geometric optimization of the experimental setup, a program generating the 3D geometry has been built in *python*. It takes the spherical coordinates of the center of each detector, the position (X, Y, Z) of the reaction point and the beam orientation as inputs. From these data, it computes the central angle and the solid angle subtended by each pixel of each telescope.

4.1 Solid angle (Ω) optimization

In order to compute the solid angle (Ω), it is necessary to calculate the coordinates of three corners (A, B, C) for each pixel, using a coordinate system centered on the target. Each pixel is then divided into $m \times n$ smaller pixels with coordinates (A_{ij}, B_{ij}, C_{ij}), where $i \in 0, ..., n$ and $j \in 0, ..., m$ and $m = n = 100$, and these smaller pixels are treated as differential areas. The coordinates of each smaller pixel can be calculated using equation 1.

$$Pixel_{ij} = \left(A_{ij}, B_{ij}, C_{ij}\right) = \begin{cases} A_{ij} = A + i\frac{\overrightarrow{d_{AB}}}{n} + j\frac{\overrightarrow{d_{AC}}}{m} \\ B_{ij} = A + (i+1)\frac{\overrightarrow{d_{AB}}}{n} + j\frac{\overrightarrow{d_{AC}}}{m} \\ C_{ij} = A + i\frac{\overrightarrow{d_{AB}}}{n} + (j+1)\frac{\overrightarrow{d_{AC}}}{m} \end{cases} \quad (1)$$

The normal vector (Eq. 2) and center (Eq. 3) of each smaller pixel is computed using the coordinates obtained above. The vector going from the pixel center to the target center ($\overrightarrow{r_{ij}} = C_{ij} - Target$) is then calculated, along with the modulus of that vector ($r_{ij} = |\overrightarrow{r_{ij}}|$), which is the distance between the target and pixel center.

$$\overrightarrow{n_{ij}} = \overrightarrow{A_{ij}B_{ij}} \times \overrightarrow{A_{ij}C_{ij}} \quad (2)$$

$$Center_{ij} = \left(\frac{C_{x,ij} + B_{x,ij}}{2}, \frac{C_{y,ij} + B_{y,ij}}{2}, \frac{C_{z,ij} + B_{z,ij}}{2}\right) \quad (3)$$

To compute the area of each smaller pixel, the pixel area is multiplied by the cosine of the angle between the normal vector ($\overrightarrow{n_{ij}}$) and the vector going from the pixel center to the target center ($\overrightarrow{r_{ij}}$), as $\overrightarrow{n_{ij}}$ is not parallel to $\overrightarrow{r_{ij}}$. The effective pixel area is given by equation 4:

$$S_{ij} = \left|\overrightarrow{A_{ij}B_{ij}}\right| \left|\overrightarrow{A_{ij}C_{ij}}\right| \cos\varphi_{ij} \quad (4)$$

where φ_{ij} is the angle between $\overrightarrow{n_{ij}}$ and $\overrightarrow{r_{ij}}$, and can be calculated using the dot product of these two vectors.

$$\overrightarrow{n_{ij}} \cdot \overrightarrow{r_{ij}} = \left|\overrightarrow{n_{ij}}\right| \left|\overrightarrow{r_{ij}}\right| \cos\varphi_{ij} \; ; \; \cos\varphi_{ij} = \frac{\overrightarrow{n_{ij}} \cdot \overrightarrow{r_{ij}}}{\left|\overrightarrow{n_{ij}}\right| \left|\overrightarrow{r_{ij}}\right|} \quad (5)$$

The solid angle for each smaller pixel is calculated using equation 6. This equation involves computing α_{ij} and β_{ij}, which are the half-lengths of the sides of the smaller pixel divided by the distance between the target and the pixel center, $\alpha_{ij} = \frac{\left|\overrightarrow{A_{ij}B_{ij}}\right|}{2r_{ij}}$ and $\beta_{ij} = \frac{\left|\overrightarrow{A_{ij}C_{ij}}\right|}{2r_{ij}}$. Since detector pixels are very small, they are treated as surface differentials, and so equation 6 can be approximated using only the first order term (equation 7).

$$\Omega_{ij} = 4 \arctan\left(\frac{\alpha_{ij}\beta_{ij}}{\sqrt{1 + \alpha_{ij}^2 + \beta_{ij}^2}}\right) \quad (6)$$

$$\Omega_{ij} = 4\alpha_{ij}\beta_{ij} = \frac{S_{ij}}{r_{ij}^2} = \frac{\left|\overrightarrow{A_{ij}B_{ij}}\right| \left|\overrightarrow{A_{ij}C_{ij}}\right| \cos\varphi_{ij}}{\left|\overrightarrow{r_{ij}}\right|^2} \quad (7)$$

The total solid angle of the detector is the sum the solid angle of each pixel (Eq. 8):

$$\Omega = \sum_{ij} \Omega_{ij} = \sum_{ij} \frac{S_{ij}}{r_{ij}^2} = \sum_{ij} \frac{\left|\overrightarrow{A_{ij}B_{ij}}\right| \left|\overrightarrow{A_{ij}C_{ij}}\right| \cos\varphi_{ij}}{\left|\overrightarrow{r_{ij}}\right|^2} \quad (8)$$

4.2 Optimizer

Once all the variables are computed the program returns θ, ϕ and Ω associated to the index of each pixel. From these data, the cross section and the ratio with respect to Rutherford are recalculated. The optimizer is based on Gradient Descent method with a loss function of normalized χ^2 to optimize the computing time.

The hit patterns of telescope A has been used to optimize the geometry due to the fact that the largest statistic was present in the two front telescopes (A and B) and telescope A seems the most centered one, as shown in Fig. 4. On the other hand, telescope B seems off-centered so its position has to be optimized independently.

The parameters obtained for the reaction point position and beam orientation are presented in Tab. 2. And the effective angles are given in Tab. 1. The parameter space was constrained between ±5 *mm* for X and Y, and ±3° for α and β.

Table 2. Parameters obtained after optimization of the geometry. Coordinates X and Y of the reaction point and rotations of the beam around X axis (α) and Y axis (β) using the right-hand rule.

Telescope	X (*mm*)	Y (*mm*)	α (°)	β (°)
A, F, E, D	-2.5	-2	0.5	1.5
B	4.5	-4.5	-1.5	3

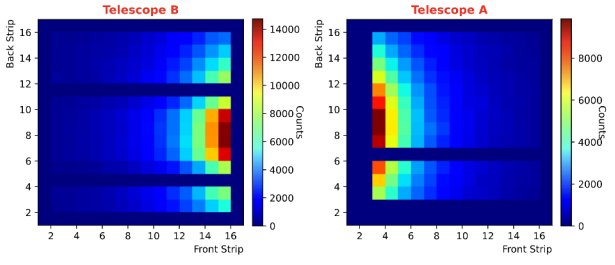

Figure 4. Hit maps of two front-side telescopes, where the beam comes in the middle between them. It can be seen how Telescope A is well centered around back strip 9 while Telescope B needs a geometric adjustment.

4.3 Electronic efficiency correction

One of the consequences of the high counting rate in front telescopes A and B was that telescopes F, E and D count less as expected due to the low trigger rate for detectors placed backwards. To calculate the electronic efficiency factor, the angular region that matches telescopes A and B with F (1.126), F with E (1.174) and E with D (1.426) has been used. The application of those factors in addition to the geometry optimization give the final distribution for the elastic scattering of ^{12}C on ^{208}Pb presented in Fig. 5.

5 Conclusions

We have optimized the GLORIA device for the present ^{15}C+^{208}Pb study using the ^{12}C+^{208}Pb scattering at 4.37 *MeV/u* energy well below the ^{12}C Coulomb barrier. We have determine the effective position of the ^{208}Pb target in comparison with the geometrical center of GLORIA. We have also determine the electronic response that make the distribution typical of Rutherford scattering. This normalization parameters will be used to extract the differential ^{15}C+^{208}Pb elastic cross section.

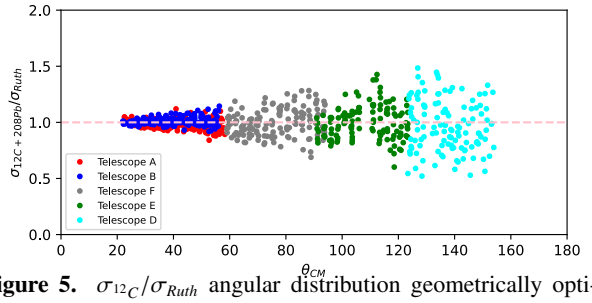

Figure 5. $\sigma_{^{12}C}/\sigma_{Ruth}$ angular distribution geometrically optimized and corrected by electronic efficiency.

Acknowledgements

We acknowledge the funding through the grant MCIN/AEI PID2019-104390GB-I00 and GIFMAN associated unit between CSIC and Universidad de Huelva.

References

[1] I. Tanihata et al., Physical Review Letters **55**, 2676 (1985)
[2] K. Riisager, Physica Scripta **2013**, 014001 (2013)
[3] T. Aumann, The European Physical Journal A-Hadrons and Nuclei **26**, 441 (2005)
[4] A. Sánchez-Benítez et al., Nuclear Physics A **803**, 30 (2008)
[5] M. Cubero et al., Physical review letters **109**, 262701 (2012)
[6] V. Pesudo et al., Phys. Rev. Lett. **118**, 152502 (2017)
[7] M. Wang et al., Chinese Physics C **36**, 1603 (2012)
[8] A. Ozawa, Nuclear Physics A **738**, 38 (2004), proceedings of the 8th International Conference on Clustering Aspects of Nuclear Structure and Dynamics
[9] A. Dobrovolsky et al., Nuclear Physics A **1008**, 122154 (2021)
[10] C. Beck et al., Physical Review C **75**, 054605 (2007)
[11] N. Keeley et al., The European Physical Journal A **50**, 1 (2014)
[12] G. Marquínez-Durán et al., Nuclear Instruments and Methods in Physics Research Section A **755**, 69 (2014)
[13] J. Díaz Ovejas, Thesis (2021)